Time of deposition refinements for key stratigraphic intervals of the Nicola Group, southern British Columbia

Mitchell G. Mihalynuk[1, a], Corey Wall[2], and Alex Zagorevski[3]

[1] British Columbia Geological Survey, Ministry of Mining and Critical Minerals, Victoria, BC, V8W 9N3
[2] Pacific Centre for Geochemical and Isotopic Research, The University of British Columbia, Earth Sciences Building, Vancouver, BC, V6T 1Z4
[3] Geological Survey of Canada, Ottawa, ON, K1A 0E8
[a] corresponding author: Mitch.Mihalynuk@gov.bc.ca

Recommended citation: Mihalynuk, M.G., Wall, C., and Zagorevski, A., 2025. Time of deposition refinements for key stratigraphic intervals of the Nicola Group, southern British Columbia. In: Geological Fieldwork 2024, British Columbia Ministry of Mining and Critical Minerals, British Columbia Geological Survey Paper 2025-01, pp. 105-118.

Abstract

Nicola Group in southern British Columbia comprises predominantly Late Triassic volcanic and derived sedimentary rocks. Comagmatic Nicola arc intrusions have produced economically important deposits of copper, gold, silver, molybdenum, and other elements during discrete periods in the Late Triassic. Advancements in defining these mineralizing events rely on accurately establishing stratigraphic-magmatic relations. This depends on geochronologic control, particularly in the extensive, regionally correlative sedimentary units that are difficult to distinguish based on rock type alone, such as parts of the Shrimpton and Elkhart formations. Detrital zircon maximum depositional age (MDA) determinations based on micro-analytical geochronological techniques such as laser ablation-inductively coupled plasma-mass spectrometry (LA-ICP-MS) are commonly too imprecise for accurate correlations. In ancient active volcanic arc environments, we can address this problem through high-precision chemical abrasion-thermal ionization mass spectroscopic (CA-TIMS) techniques to refine MDAs to times of deposition. Aided by new time of deposition (TOD) determinations, we show that following a major growth phase that ended after 224 Ma, the beginning of widespread Nicola arc incision was underway by 222.0 Ma, as recorded by deposition of the Elkhart Formation. Abrupt disruption of Nicola arc magmagenesis led to more hydrated phenocryst assemblages and ultrapotassic basalt flows by 202.6 Ma. Porphyry mineralization in the southern Nicola arc is bracketed by the 222.0 and 202.6 TOD ages, and the arc was largely extinguished by 201.3 Ma.

Keywords: Nicola arc, Quesnel terrane, porphyry copper mineralization, mineral exploration, detrital zircon, maximum depositional age, time of deposition, Triassic-Jurassic boundary, time scale, subduction initiation, volcanic arc collision

1. Introduction

Early porphyry copper exploration in British Columbia relied on recognizing broad alteration halos and colour anomalies arising from oxidation of widespread disseminated pyrite surrounding calc-alkalic Cu-Mo deposits (Lowell and Guilbert, 1970; e.g., Highland Valley**;** McMillan and Panteleyev, 1980). Much more subtle alteration halos surround alkalic Cu-Au-Ag porphyry deposits for which the Nicola arc is renowned (Barr et al., 1976; Logan and Mihalynuk, 2014). Alkalic porphyry Cu-Au-Ag deposits tend to be higher grade and are associated with near-vertical pencil-shaped stocks having cross sectional areas an order of magnitude smaller than bodies hosting calc-alkalic deposits (although they may form extensive clusters, e.g., Iron Mask (New Afton); Copper Mountain; Mount Polley). As a result, greater exploration precision may be required in their initial discovery, significantly aided by detailed volcano-stratigraphy (e.g., Mihalynuk and Diakow, 2020).

Using detrital zircon geochronology, herein we provide high-precision updates to uncertain unit boundaries in the southern Nicola arc (Fig. 1), in an area that includes the territories of many Indigenous Nations. Continuous influx of zircon-bearing ash from active volcanic arcs ensures that sedimentary basins on the volcanic arc flanks contain penecontemporaneous magmatic zircons that record the time of deposition (TOD). Large numbers of grains need to be analyzed (typically 80-300 depending on the complexity of sources) to ensure a statistically high probability of extracting and dating a population of TOD zircons. This can be economically done with laser ablation-inductively coupled plasma-mass spectrometry (LA-ICP-MS) techniques (e.g., Gehrels, 2014; Herriott et al., 2019) which permit bulk mounting, imaging and dating of tens to hundreds of zircon grains. However, low-precision is a drawback of LA-ICP-MS, in part due to the small sampling volume of individual spot analyses; the propagated errors on these tend to be large (±1 to 5% of the age of a Mesozoic zircon grain). As such, meaningful interpretations require statistical treatments (e.g., Vermeesch, 2018) to combine the youngest population of ages for determination of a maximum deposition age (MDA). Typically, tens of LA-ICP-MS U-Pb age determinations are included in a weighted mean age that may have an error envelope that spans more than 10 million years. Such MDA determinations are ineffective at resolving geological problems arising from multiple events that all occur within the 10 m.y. span of the error envelope.

To circumvent this issue, we use LA-ICP-MS to characterize the population(s) of zircon and to identify young zircons.

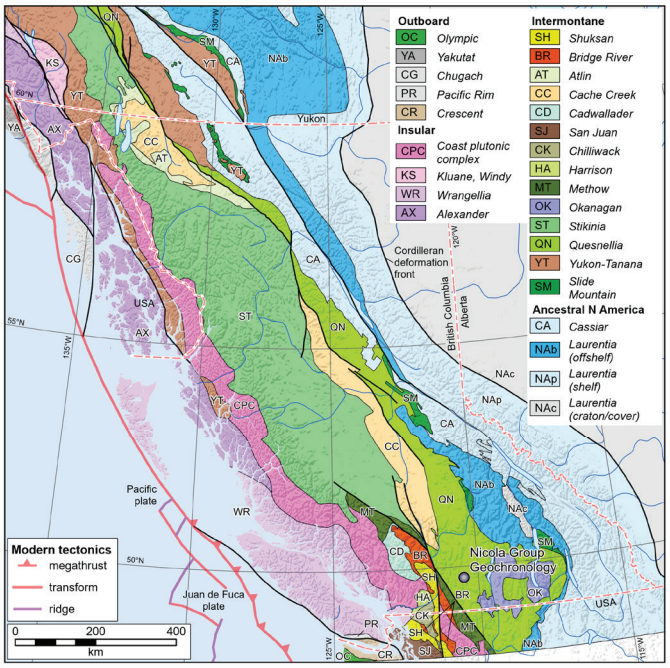

Fig. 1. Location of study area. Terranes (after Wheeler et al., 1991; Colpron and Nelson, 2011; Zagorevski et al., 2020) modified from Colpron (2020).

Young zircon grains that show clear igneous textures are then extracted and dated using a much higher precision chemical abrasion-isotope dilution-thermal ionization mass spectrometry (CA-TIMS). Two-sigma errors on the age determinations are on the order of 0.05%, a one to two order of magnitude improvement on the MDA age uncertainties, thereby providing high-precision TOD determinations. Here we report on three such age determinations from zircons extracted from sedimentary rocks at key horizons within the Nicola Group strata of southern British Columbia (Figs. 1, 2).

2. Geological setting

British Columbia is mostly underlain by accreted crustal blocks, the largest of which is the Intermontane superterrane extending the length of the province (Fig. 1; Monger et al., 1982; Wheeler and McFeely, 1987) and consists of twin arc terranes, Stikine and Quesnel (Coney et al., 1980), thought to have grown conjoined at their northern ends (Mihalynuk et al., 1994). Quesnel terrane was probably added to North America at ca.185 Ma (Archibald et al., 1983; Colpron et al., 1998; Nixon et al., 2020), followed by diachronous collision of Stikine terrane, at ca. 174 Ma in the north (Mihalynuk et al., 2004). These arc terranes are important to the economy of British Columbia because they contain large porphyry Cu-Mo and Cu-Au-Ag deposits, mostly formed in the Late Triassic, between 211 and 201 Ma. More than 90% of the known copper resources in these terranes was formed during this porphyry epoch (205 ±6 Ma; Logan et al., 2007; Logan and Mihalynuk, 2014), with the southern Quesnel terrane accounting for most of the past mining production.

Owing to the economic importance and lack of modern systematic geological surveys across key portions of Late Triassic arc rocks in southern Quesnel terrane, the British Columbia Geological Survey launched the Southern Nicola Arc Project between the producing deposits at Copper Mountain (to the south), Highland Valley (northwest) and New Afton (to the north, Fig. 2). A principal aim of the project was to update the stratigraphic and magmatic evolution of the Late Triassic porphyry belt established by earlier workers (Schau, 1968; Preto, 1972, 1979; McMillan, 1981; Monger, 1989; Monger and McMillan, 1989), taking advantage of the ever-expanding road network and more modern mapping and geochronologic techniques (Mihalynuk et al., 2014a, b, 2015a, b, 2016; Friedman et al., 2016, 2020). These studies, many including geological mapping by industry, are synthesized in Mihalynuk and Diakow (2020) and the resulting stratigraphic framework for the Nicola Group is shown in Figure. 3.

2.1. Context of new Nicola arc geochronology

Rhyolitic volcanism of the Missezula Formation marks the initiation of the Nicola arc at ca. 240 Ma (Friedman et al., 2020; late Middle Triassic, Cohen et al., 2013). The most recognizable and thickest portions of the Nicola Group overlie the Missezula Formation and comprise the hallmark augite porphyries of the Iron Mountain Formation (see also unit 3 of Schiarizza, 2019). The overlying Selish Formation comprises shallow-water limestone intercalated with thin volcaniclastic rhyolite (223-225 Ma; Mihalynuk et al., 2016) and augite-phyric basalt. It was deposited as the arc grew above sea level. The Allison batholith of the Mount Pike suite (223 Ma, Mihalynuk et al., 2016) intruded the western arc axis of the study area (Fig. 2) and was comagmatic with the Selish Formation. The Selish Formation is unconformably overlain by terrigenous, deeply oxidized, coarse polylithic conglomerate and sandstone of the Elkhart Formation, locally including accumulations of mafic and intermediate volcanic flows and breccias 100s of m thick. Fresh hornblende from a flow near the top of the succession yielded an $^{40}Ar/^{39}Ar$ cooling age of ca. 210 Ma (Fig. 3; Gabites and Mihalynuk, 2025). However, the age of the base of the Elkhart Formation was previously only loosely constrained as younger than the Selish Formation (223 Ma) and with an imprecise MDA of 222 Ma (Mihalynuk et al., 2016). The same sample (LDi14-60-3) is revisited in this study.

The Shrimpton Formation caps the Nicola Group and marks a significant change in the typical pyroxene±hornblende phenocryst assemblage of the volcanic rocks. The Shrimpton Formation is predominantly conglomeratic, with a tuffaceous component that commonly includes pyroclastic biotite, apatite and quartz. We present LA-ICP-MS and CA-TIMS age data for a sample collected low in the Shrimpton Formation (sample MMI17-9-3). Before this study, the onset of Shrimpton Formation deposition was constrained by the 210 Ma cooling age in the underlying Elkhart Formation (Gabites and Mihalynuk, 2025), plus an imprecise MDA of 207 Ma low in the Shrimpton stratigraphy (Mihalynuk et al., 2025). The age of

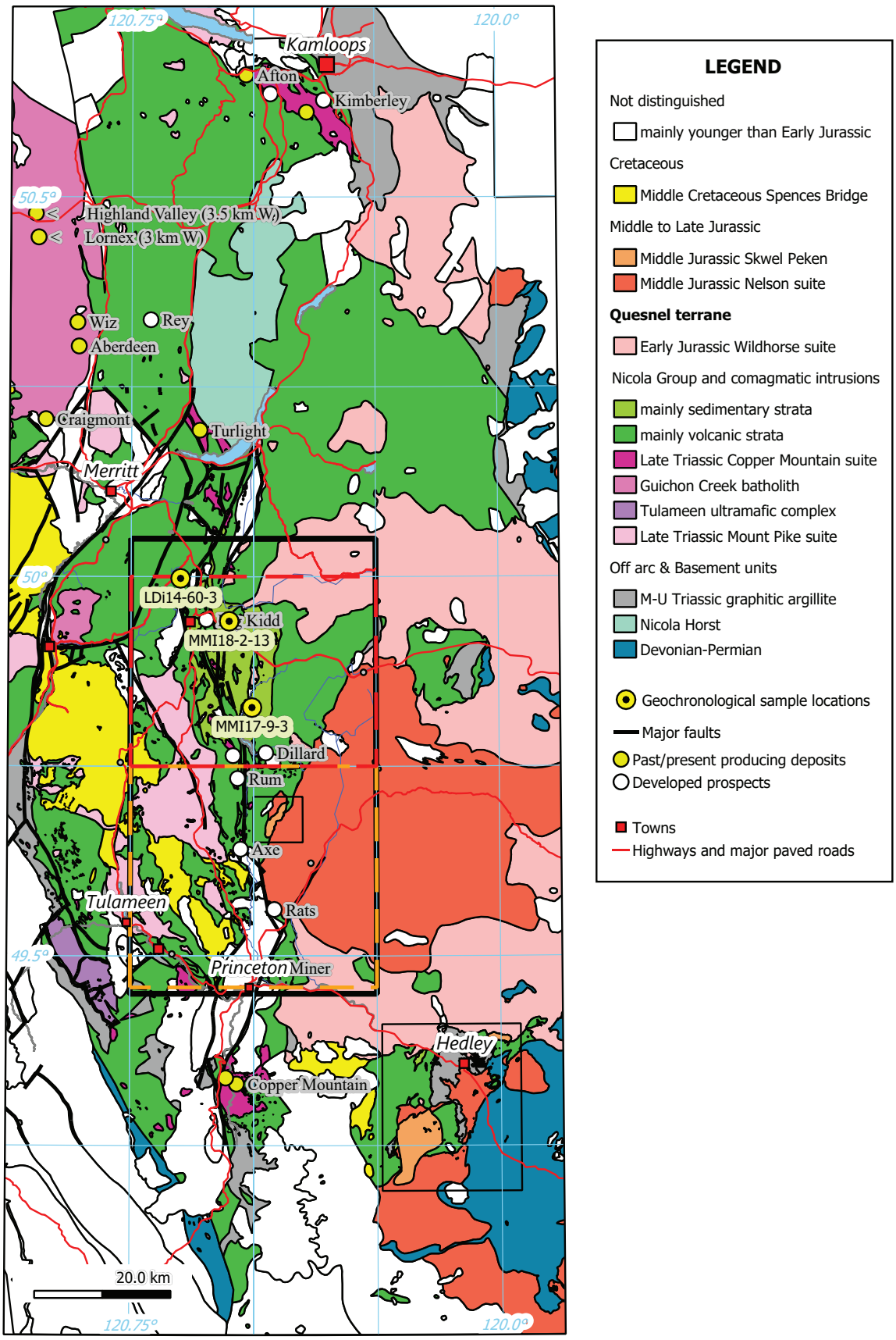

Fig. 2. Generalized geology of southern Nicola arc with sample locations shown. Rectangles outline areas mapped at 1:50,000 scale by Mihalynuk et al. (2014a, 2015a; orange and red dashed outlines), updated in Mihalynuk and Diakow, 2020 (thick black outline).

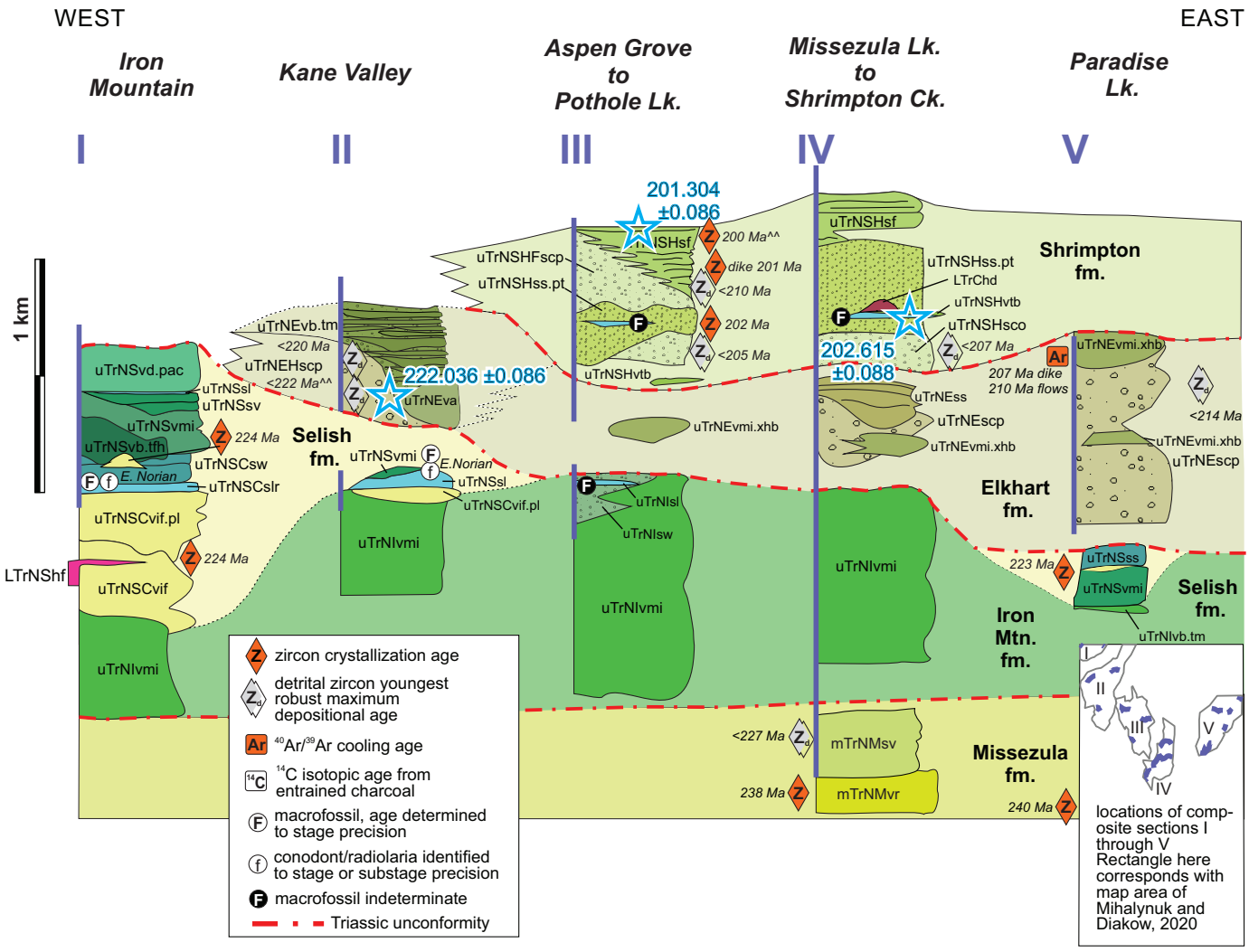

Fig. 3. Comparative lithostratigraphy for subregions across the northern study area as shown by the lower right inset (after Mihalynuk and Diakow, 2020). Correlations and lateral facies changes are shown together with supporting age data, with blue stars denoting sample locations and derived time of deposition determinations presented here. Microfossil age determinations (lower case 'f' in circle are from Orchard (1990) based on conodonts found together with macrofossils (upper case 'F' in circle). Unit designations have the following prefixes: Missezula Formation, MTrNM; Iron Mountain Formation, uTrNI; Selish Formation, uTrNS (Castillion Creek members are denoted uTrNSC); Elkhart Formation, uTrNE (Harmon members are denoted uTrNEH); Shrimpton Formation, uTrNSH (Fairweather Hills members denoted uTrNSHF). Unit designation suffixes in lower case are, first letter: h, hypabyssal; s, sedimentary; v, volcanic. Second letters of suffix denote: a, andesite; b, basalt; c, conglomerate; d (following v), dacitic; d (following h), dioritic; i, intermediate; l, limestone; m, mafic; r, rhyolite; w, wacke. Third letters of suffix denote: b (following c), basal; f (following v), felsic; f (following s), fine-grained; i, intermediate; l, limestone; o (following c), oligomictic; p (following c), polymictic; r, reefal; s, sandstone; t, trachy. Dot extension of suffix denote distinctive characteristics: pt/pl, pyroclastic-tuff/lapilli tuff; tm, textural-megacrystic; xhb, phenocrystic hornblende.

the top of the Shrimpton Formation was formerly constrained by a tuff layer yielding zircons with a weighted mean LA-ICP-MS age of 200.2 ±1.1 Ma, and a young error limit that extended into the Early Jurassic. Using the same sample (MMI18-2-13), below we provide a precise CA-TIMS age for this youngest dated volcanic rock in the southern Nicola arc.

3. U-Pb zircon geochronology methods

3.1. LA-ICP-MS analyses

Our set-up for LA-ICP-MS work followed the methods in Friedman et al. (2020). After rock samples underwent standard mineral separation procedures, zircons were handpicked in alcohol and mounted in epoxy, along with reference materials. Grain mounts were then wet ground with carbide abrasive paper and polished with diamond paste. Next, cathodoluminescence (CL) imaging was carried out (Fig. 4) on a Philips XL-30 scanning electron microscope (SEM) equipped with a Bruker Quanta 200 energy-dispersion X-ray microanalysis system at the Electron Microbeam/XRay Diffraction Facility (EMXDF) at the University of British Columbia. An operating voltage of 15 kV was used, with a spot diameter of 6 µm in automated CL mode, and a peak count time of 17-27 seconds. After removal of the carbon coat, the grain mount surface was washed with mild soap and rinsed with high-purity water. Before analysis,

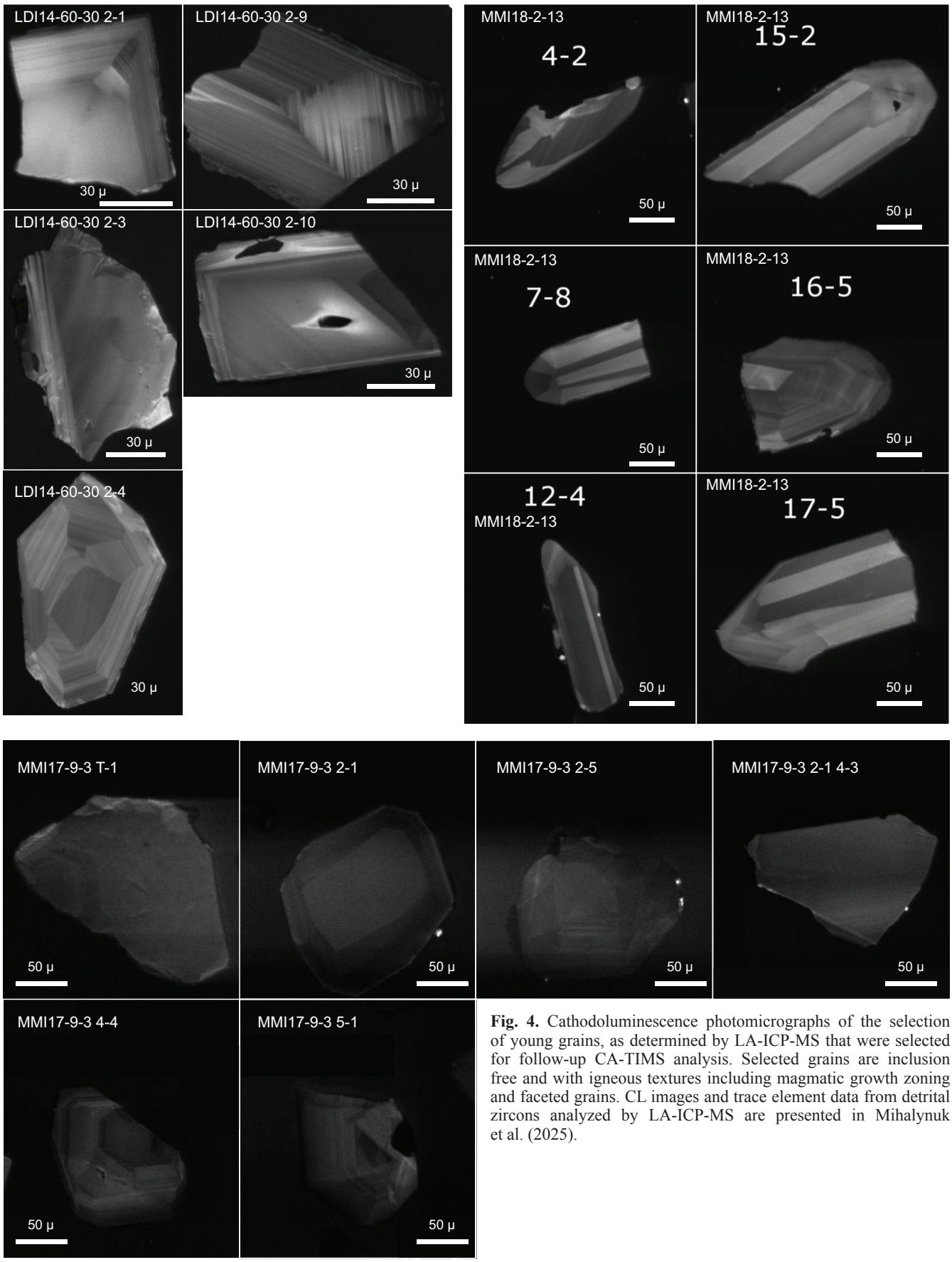

Fig. 4. Cathodoluminescence photomicrographs of the selection of young grains, as determined by LA-ICP-MS that were selected for follow-up CA-TIMS analysis. Selected grains are inclusion free and with igneous textures including magmatic growth zoning and faceted grains. CL images and trace element data from detrital zircons analyzed by LA-ICP-MS are presented in Mihalynuk et al. (2025).

the grain mount surface was cleaned with 3 N HNO_3 acid and again rinsed with high-purity water to remove any surficial Pb contamination that could interfere with the early portions of the spot analyses.

Analyses were conducted using a Resonetics RESOlution M-50-LR, which contains a Class I laser device equipped with a UV excimer laser source (Coherent COMPex Pro 110, 193 nm, pulse width of 4 ns) and a two-volume cell designed and developed by Laurin Technic Pty. Ltd. (Australia). This sample chamber allowed for the investigation of several grain mounts in one analytical session. The laser path was fluxed by N2 to ensure better stability. Ablation was carried out in a cell with a volume of approximately 20 cm^3 and a He gas stream that ensured better signal stability and lower U-Pb fractionation (Eggins et al., 1998). The laser cell was connected via a Teflon squid to an Agilent 7700x quadrupole ICP-MS housed at the Pacific Centre for Isotopic and Geochemical Research. A pre-ablation shot was used to ensure that the spot area on the grain surface was contamination-free. Samples and reference materials were analyzed for 36 isotopes: ^{7}Li, ^{29}Si, ^{31}P, ^{43}Ca, ^{45}Sc, ^{49}Ti, Fe (^{56}Fe, ^{57}Fe), ^{89}Y, ^{91}Zr, ^{93}Nb, ^{95}Mo, ^{98}Mo, ^{139}La, ^{140}Ce, ^{141}Pr, ^{146}Nd, ^{147}Sm, ^{153}Eu, ^{157}Gd, ^{159}Tb, ^{163}Dy, ^{165}Ho, ^{166}Er, ^{169}Tm, ^{172}Lu, ^{177}Hf, ^{181}Ta, ^{202}Hg, Pb (^{204}Pb, ^{206}Pb, ^{207}Pb, ^{208}Pb), ^{232}Th, and U (^{235}U, ^{238}U) with a dwell time of 0.02 seconds for each isotope. Pb/U and Pb/Pb ratios were determined on the same spots along with trace element concentrations. These isotopes were selected based on their relatively high natural abundances and absence of interferences. The settings for the laser were: spot size of 34 µm with a total ablation time of 30 seconds, frequency of 5 Hz, fluence of 5 J/cm^2 , power of 7.8 mJ after attenuation, pit depths of approximately 15 µm, He flow rate of 800 ml/min, N_2 flow rate of 2 ml/min, and a carrier gas (Ar) flow rate of 0.57 l/min. Reference materials were analyzed throughout the sequence to allow for drift correction and to characterize downhole fractionation for Pb/U and Pb/Pb isotopic ratios. For trace elements, NIST 612 glass was used for both drift correction and trace element calibration, with sample spacing between every five to eight unknowns, and ^{90}Zr was used as the internal standard assuming stoichiometric values for zircon. NIST 610 glass was analyzed after each NIST 612 analysis and used as a monitor reference material for trace elements. For U-Pb analyses, natural zircon reference materials were used, including Plešovice (Sláma et al., 2008; 337.13 ±0.33 Ma) or 91500 (Wiedenbeck et al., 1995; ^{207}Pb/^{206}Pb: 1065.4 ±0.3 Ma; ^{206}Pb/^{238}U 1062.4 ±0.4 Ma) as the internal reference material and both Temora2 (Black et al., 2004; 416.78 ±0.33 Ma) and Plešovice and/or 91500 as monitoring reference materials; the zircon reference materials were placed between the unknowns in a similar fashion as the NIST glasses. Raw data were reduced using the Iolite 3.4 extension (Paton et al., 2011) for Igor ProTM, yielding concentration values, Pb/U and Pb/Pb dates, and their respective propagated uncertainties. Final interpretation and plotting of the analytical results employed the ISOPLOT software of Ludwig (2003).

3.2. Grain selection, preparation, and CA-TIMS analyses

U-Pb dates were obtained by the chemical abrasion isotope dilution thermal ionization mass spectrometry (CA-TIMS) method, modified after Mattinson (2005), from analyses composed of single zircon grains. A population of the youngest grains dated by LA-ICP-MS were selected based on their igneous character as indicated by cathodoluminesce imaging (Fig. 4). Selected zircons were plucked from their mounts and transferred into 5 µL microcapsules, placed in a large-capacity Parr vessel, and partially dissolved in 120 µL of 29 M HF for 12 h at 180°C or 190°C. The zircons were returned to 3 ml Teflon PFA beakers, the HF was removed, and immersed in 3.5 M HNO_3, ultrasonically cleaned for an hour, and fluxed on a hotplate at 80°C for an hour. The HNO_3 was removed, and the zircons were rinsed twice in ultrapure H_2O before being reloaded into the 300 µL Teflon PFA microcapsules (rinsed and fluxed in 6 M HCl during sonication and washing of the zircon) and spiked with the EARTHTIME mixed ^{233}U-^{235}U-^{205}Pb tracer solution (ET535). Zircon was dissolved in Parr vessels in 120 µL of 29 M HF with a trace of 3.5 M HNO_3 at 220°C for 48 h, dried to fluorides, and re-dissolved in 6 M HCl at 180°C overnight. Solutions were subsequently dried down and redissolved in 60 µL of 3 M HCl to convert to $PbCl_{3-}$, UO_2Cl_{3-}, and UCl_6-ions. U and Pb were separated from the zircon matrix using an HCl-based anion-exchange chromatographic procedure (Krogh, 1973). Pb was eluted with 200 µL of 6 M HCl and U with 250 µL of MQ-H_2O into the same beaker and dried with 2 µL of 0.05 N H_3PO_4.

Pb and U were loaded on a single outgassed Re filament in 5 µL of a silica gel/phosphoric acid mixture (Gerstenberger and Haase, 1997), and U and Pb isotopic measurements were made on a Nu Instruments thermal ionization mass spectrometer equipped with high-sensitivity 10^{13} Ω resistors Faraday detectors and an ion-counting Daly detector. Pb isotopes were measured in static Faraday mode with mass 204 on the Daly detector for 200 cycles. Mass fractionation was determined using repeat measurements of standard material NBS-981 solution that has equal atom ^{208}Pb and ^{206}Pb and thus measures fractionation directly (0.16 ±0.01% amu^{-1}; 1σ). Transitory isobaric interferences due to high-molecular-weight organics, particularly on ^{204}Pb and ^{207}Pb, disappeared within approximately 20 cycles. Uranium was analyzed as UO ions in static Faraday mode on 10^{13} Ω resistors for 200 cycles and corrected for isobaric interference of ^{233}U^{18}O^{16}O on ^{235}U^{16}O^{16}O with and ^{18}O/^{16}O ratio of 0.00206. U mass fractionation was corrected using the known ^{233}U/^{235}U ratio of the tracer solution.

U-Pb dates and uncertainties were calculated using the algorithms of Schmitz and Schoene (2007); calibration of ET535 tracer solution (Condon et al., 2015) of ^{235}U/^{205}Pb=100.233, ^{233}U/^{205}Pb=0.99506, and ^{205}Pb/^{204}Pb=11268; U decay constants recommended by Jaffey et al. (1971); and of ^{238}U/^{235}U=137.818 (Hiess et al., 2012). The ^{206}Pb/^{238}U ratios and dates were corrected for initial ^{230}Th disequilibrium using $_{DTh/U}$=0.20 ±0.05 (1σ) and the algorithms of Crowley et al. (2007), resulting in an increase in the ^{206}Pb/^{238}U dates of ~0.09 Ma. All common Pb in analyses

was attributed to laboratory blank and subtracted based on the measured laboratory Pb isotopic composition and associated uncertainty. Common Pb values vary from grain to grain, as reported in Table 1. U blanks are estimated at 0.013 pg. Weighted mean $^{206}Pb/^{238}U$ dates are calculated from equivalent dates (probability of fit >0.05) using Isoplot 3.0 (Ludwig, 2003).

4. Results

CA-TIMs analytical results are presented in Table 1; cathodoluminescence images and trace element data from detrital zircons analyzed by LA-ICP-MS are presented in Mihalynuk et al. (2025). Results are discussed in the following sections, together with the immediate geological setting and implications of the age data.

4.1. Elkhart Formation, Kane Valley area (LDi14-60-3; Lat. 49.99790°N, Long. -120.64900°E)

Sample LDi14-60-3 was collected from the base of a redbed sandstone and bladed feldspar porphyry flow section. Conglomeratic sandstone and tuffaceous siltstone layers (Fig. 3, section II, unit uTrNEvb.tm) are exposed along a dirt road that forms part of the Nicola Nordic Ski Club cross-country ski trail network in the Kane Valley. Clean outcrop was exposed along one of the roadcuts at the site shown in Figure 5a and a ~15 kg block of coarse sandstone was collected. The sample locality is approximately 150 m stratigraphically below the lowest exposures of a distinctive succession of coarse bladed feldspar flows (Fig. 5b) that range between 5 and 50 m thick (Fig. 3, section II, unit uTrNEvb.tm).

LA-ICP-MS analysis of a representative population of zircons extracted from the sample (n=64) yielded an age distribution with a mode at 220 Ma (Mihalynuk et al., 2016). Mihalynuk et al. (2016) used a five-grain subpopulation of youngest zircons to interpret the likely MDA at ca. 213 Ma (Fig. 6a). Another sample from this unit was previously collected approximately 3 km along strike to the north-northeast (12JLO-51-47 in Mihalynuk et al., 2015a, b). It yielded an age distribution with a mode of 222 Ma (the youngest reliable zircon grain was erroneously interpreted as 208.0 ±7.6 Ma in Mihalynuk et al., 2015a).

Our new time of deposition of 222.036 ±0.086 Ma is based on the youngest of the six grains dated (Fig. 6b). It is consistent with the LA-ICP-MS modes of the two earlier age determinations rather than the young interpreted subpopulation or youngest 'reliable' zircon MDAs (Fig. 6a), but with an age uncertainty that is almost two orders of magnitude smaller.

4.2. Lower part of Shrimpton Formation, Shrimpton Creek area (MMI17-9-3; 49.82763°N, -120.50219°E)

Sample MMI17-9-3 was collected from a low ditch along a logging road that parallels Shrimpton Creek about 3 km from Missezula Lake. About 10 kg of slabby, fist-sized blocks of sandstone were collected.

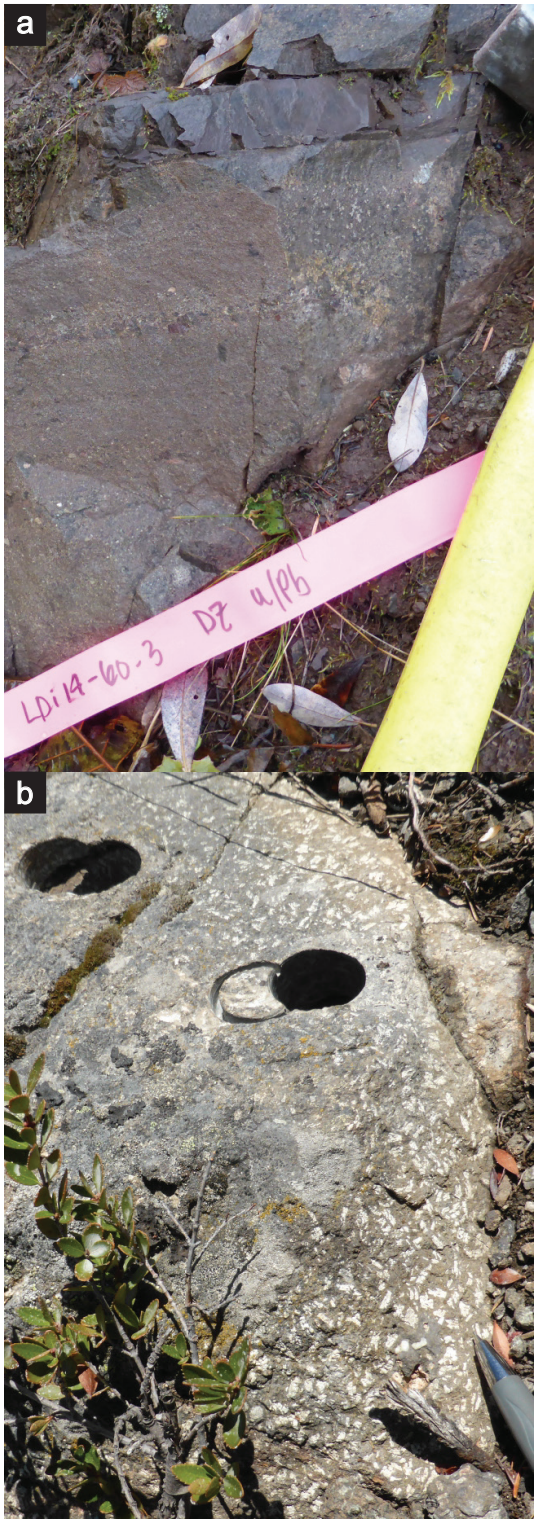

Fig. 5. **a)** Outcrop from which sample LDI14-60-3 was collected for detrital zircon separation. These are typical maroon, oxidized volcanic pebble and granule conglomerate and sandstone (base of outcrop) with fine ash tuff rich interbeds (beneath head of hammer). Pink flagging tape is ~25 mm wide. **b)** An age determination from sample site constrains the age of an overlying succession of 5-50 m thick bladed feldspar porphyry flows that has been extensively drilled for paleomagnetic study. Pen and drill holes for scale: the inner core of the drill holes is ~25 mm.

Table 1. CA-TIMS U-Pb isotopic data.

	Compositional Parameters						Radiogenic Isotope Ratios								Isotopic Ages					
Sample (a)	Th/U (b)	$^{206}Pb^*$ x10^{-13} mol (c)	mol % $^{206}Pb^*$ (c)	Pb^*/Pb_c (c)	Pb_c (pg) (c)	$^{206}Pb/^{204}Pb$ (d)	$^{208}Pb/^{206}Pb$ (e)	$^{207}Pb/^{206}Pb$ (e)	% err (f)	$^{207}Pb/^{235}U$ (e)	% err (f)	$^{206}Pb/^{238}U$ (e)	% err (f)	corr. coef.	$^{207}Pb/^{206}Pb$ (g)	± (f)	$^{207}Pb/^{235}U$ (g)	± (f)	$^{206}Pb/^{238}U$ (g)	± (f)
LDI14-60-3																				
2-1	0.636	0.3105	99.37%	49	0.16	2881	0.202	0.05062	0.175	0.244776	0.191	0.035089	0.041	0.490	222.4	4.04	222.32	0.38	222.317	0.090
2-3	0.775	0.3051	99.45%	58	0.14	3260	0.246	0.05064	0.166	0.244922	0.184	0.035093	0.044	0.515	223.5	3.83	222.44	0.37	222.345	0.097
2-4	0.919	0.8329	99.72%	120	0.19	6516	0.292	0.05063	0.076	0.245161	0.095	0.035137	0.042	0.627	222.8	1.76	222.64	0.19	222.621	0.093
2-9	0.503	0.4221	99.39%	49	0.21	2973	0.160	0.05064	0.156	0.244722	0.173	0.035068	0.040	0.519	223.3	3.60	222.28	0.34	222.186	0.086
2-10	0.682	0.9648	99.76%	133	0.19	7651	0.217	0.05063	0.074	0.244753	0.091	0.035078	0.039	0.614	222.9	1.72	222.30	0.18	222.249	0.085
2-15	0.748	0.5610	99.62%	84	0.18	4773	0.238	0.05064	0.090	0.244575	0.106	0.035043	0.039	0.570	223.5	2.08	222.16	0.21	**222.036**	**0.086**
MMI17-9-3																				
T-1	1.151	0.3012	99.30%	50	0.18	2576	0.366	0.05019	0.185	0.220878	0.203	0.031930	0.044	0.508	202.9	4.29	202.64	0.37	**202.615**	**0.088**
2-1	1.147	0.3211	99.35%	54	0.17	2766	0.365	0.05021	0.164	0.221748	0.182	0.032044	0.044	0.505	203.8	3.81	203.36	0.34	203.327	0.087
2-5	0.412	0.2344	99.25%	39	0.15	2393	0.131	0.05022	0.239	0.221683	0.258	0.032032	0.041	0.531	203.9	5.54	203.31	0.48	203.256	0.083
4-3	0.839	0.2382	99.15%	38	0.17	2133	0.267	0.05020	0.285	0.221453	0.306	0.032009	0.044	0.528	203.2	6.62	203.12	0.56	203.110	0.089
4-4	0.920	0.3718	99.29%	47	0.22	2534	0.293	0.05021	0.172	0.221140	0.188	0.031960	0.042	0.494	203.5	3.98	202.86	0.35	202.802	0.083
5-1	0.866	0.2885	99.21%	41	0.19	2279	0.275	0.05021	0.215	0.222591	0.234	0.032164	0.044	0.501	203.9	5.00	204.06	0.43	204.081	0.088
MMI18-2-13																				
7-8	0.541	0.2735	99.39%	50	0.14	2981	0.172	0.05021	0.193	0.221816	0.210	0.032057	0.042	0.485	203.5	4.49	203.42	0.39	203.410	0.083
4-2	0.542	0.3353	99.33%	45	0.19	2706	0.172	0.05022	0.191	0.222893	0.210	0.032203	0.045	0.511	204.2	4.43	204.32	0.39	204.322	0.090
12-4	0.614	0.1289	98.06%	16	0.21	931	0.195	0.05021	0.531	0.221359	0.566	0.031992	0.055	0.668	203.5	12.32	203.04	1.04	203.00	0.11
15-2	0.499	0.1920	98.77%	24	0.20	1462	0.159	0.05018	0.322	0.219346	0.346	0.031720	0.044	0.590	202.1	7.48	201.37	0.63	**201.304**	**0.086**
17-5	0.568	0.1417	98.56%	21	0.17	1249	0.181	0.05022	0.391	0.222492	0.419	0.032144	0.050	0.602	204.3	9.08	203.98	0.78	203.95	0.10
16-5	0.485	0.2027	98.96%	28	0.18	1735	0.154	0.05020	0.332	0.221612	0.355	0.032034	0.048	0.549	203.1	7.69	203.25	0.65	203.267	0.096

(a) **2-15, T-1** etc. are labels for single zircon grains or fragments annealed and chemically abraded after Mattinson (2005); **bold** indicates youngest zircon and time of deposition.
(b) Model Th/U ratio iteratively calculated from the radiogenic 208Pb/206Pb ratio and 206Pb/238U age.
(c) Pb* and Pbc represent radiogenic and common Pb, respectively; mol % $^{206}Pb^*$ with respect to radiogenic, blank and initial common Pb.
(d) Measured ratio corrected for spike and fractionation only. Fractionation calculated from repeated measurements of NBS-982 for Pb ratios and double spike for U ratios.
(e) Corrected for fractionation, spike, and common Pb; all common Pb was assumed to be procedural blank: 206Pb/204Pb = 18.042 ± 0.61%; 207Pb/204Pb = 15.537 ± 0.52%; 208Pb/204Pb = 37.686 ± 0.63% (all uncertainties 1-sigma).
(f) Errors are 2-sigma, propagated using the algorithms of Schmitz and Schoene (2007).
(g) Calculations are based on the decay constants of Jaffey et al. (1971) and 238U/235U = 137.818. 206Pb/238U and 207Pb/206Pb ages corrected for initial disequilibrium in 230Th/238U using Th/U(magma) = 2.8 ± 0.05 (1s).
(h) Age uncertainties reported as ± analytical [+decay constant]; MSWD = mean squared weighted deviation.

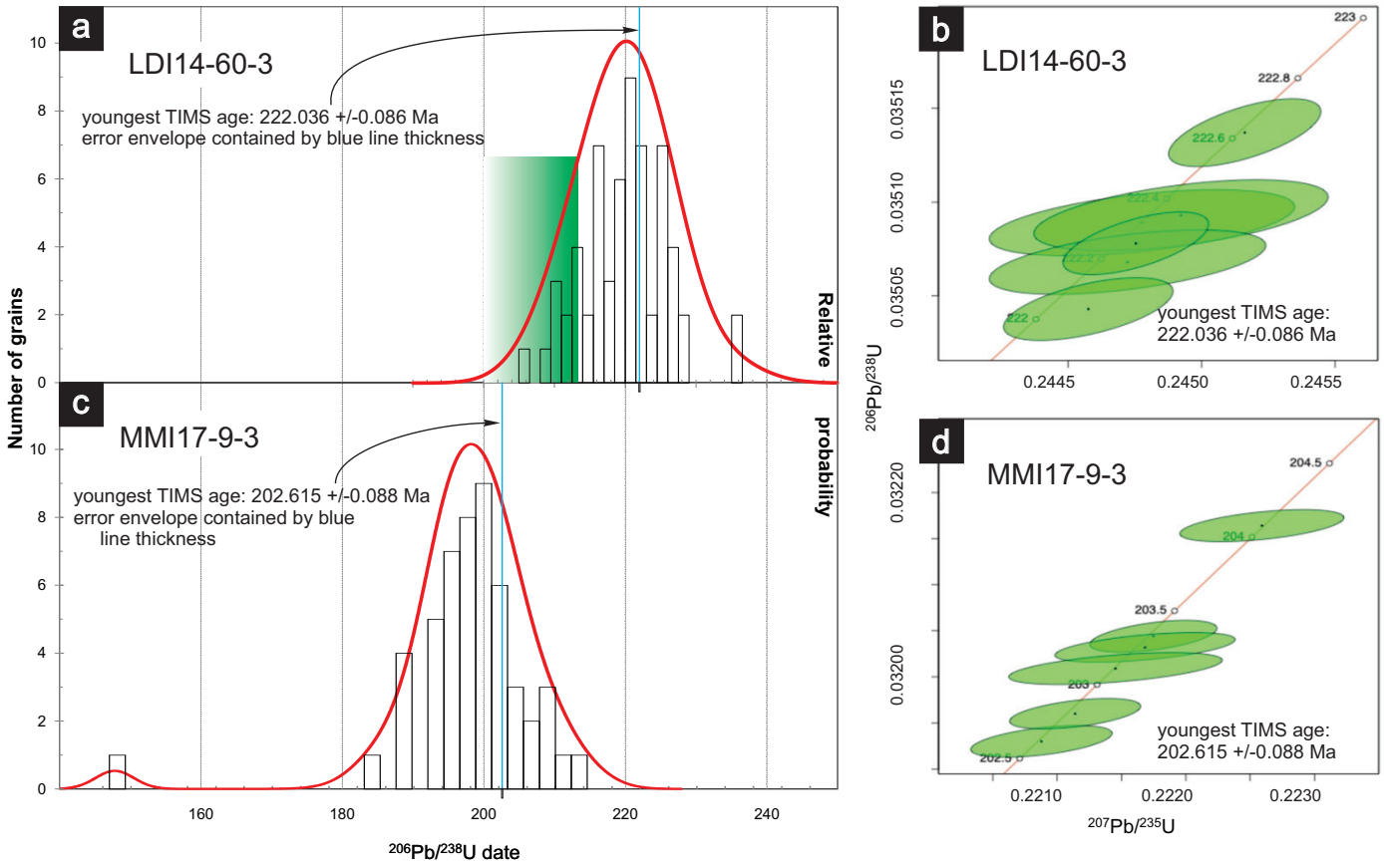

Fig. 6. Age data plotted for samples LDI14-60-3 **a)** Age distribution, **b)** Concordia, and MMI17-9-3, **c)** Age distribution, and **d)** Concordia, showing the difference between LA-ICP-MS analysis of detrital zircon populations and CA-TIMS analyses of the youngest grains selected from both samples. Shaded green area in a) (LDI14-60-3 plot) represents the MDA subpopulation age (<213 Ma) reported by Mihalynuk et al. (2016). Error envelopes of CA-TIMS analyses are contained by the blue line thickness (error specifically denoted by box below the abscissae).

The sample is part succession that signals a significant change in the petrogenesis of the Nicola arc volcanic rocks. Hallmark augite-plagioclase ±hornblende-phyric units are overlain by monzonite clast-bearing conglomerate, calcareous sedimentary rocks, analcime basalt, and quartz-biotite-apatite-feldspar-porphyritic tuff and epiclastic rocks.

Characteristic of the base of the Shrimpton Formation are resistant, massive conglomerate lenses predominantly containing pink to orange-weathering porphyritic monzonitic clasts (Fig. 7a) and lesser basalt clasts (unit uTrNSHsco, Fig. 2; Fig. 3, section IV). These lenses are up to 320 m thick, with strike extents of more than 10 km, and are enclosed in coarse sandstone. Monzonitic clasts are compositionally uniform, containing ~20% medium-grained, tabular feldspar, 5-10% prismatic hornblende, and are resistant in comparison to the ash-rich matrix that contains pyroxene, hornblende, and up section, increasing contents of biotite, apatite and sparse quartz grains. Biotite occurs as medium-grained, copper-coloured (ranging to shiny grey or green) altered booklets, typically less than 0.5% of the rock, but is locally concentrated (to ~4%) on some bedding planes. Medium to fine-grained quartz eyes are subhedral, smoky, and irregularly distributed (<0.1%, rarely to 2%). Apatite is typically red-stained prisms less than 1 mm in diameter. Carbonaceous plant remains and rare crinoid fossils indicate a shallow marine setting.

Above the conglomerate-bearing strata, limestone, limestone breccia, and carbonate-cemented tuffaceous sandstone (Fig. 7b) occur within an intermittently exposed, approximately 5 m thick interval in the sandstone/tuffite unit. Beds are disrupted and contain blocky, brecciated (Fig. 7b), or discontinuous, analcime-titanaugite-phyric basalt flows that average ~30 cm thick. Thicker flows occur along strike, both to the north and south, with southern sections of massive analcime flows attaining thicknesses of 10-20 m. Medium to coarse-grained, black titanaugite typically comprises 15-25%, and subequant (dodecahedral) analcime is normally beige and comprises 10-15% of the rock (Fig. 7c).

Fifty-three grains of the lower Shrimpton Formation sandstone sample MMI17-9-3 were analyzed and the resultant probability distribution shows a peak at 200 Ma with an age mode at 202 Ma (using 4 m.y. bins). A young outlier with an apparently concordant age ($^{206}Pb/^{238}U$ age of 149.7 ±5.4 Ma) was treated as contamination. Six grains from the young side of the age distribution were analyzed by CA-IDTIMS. Individual

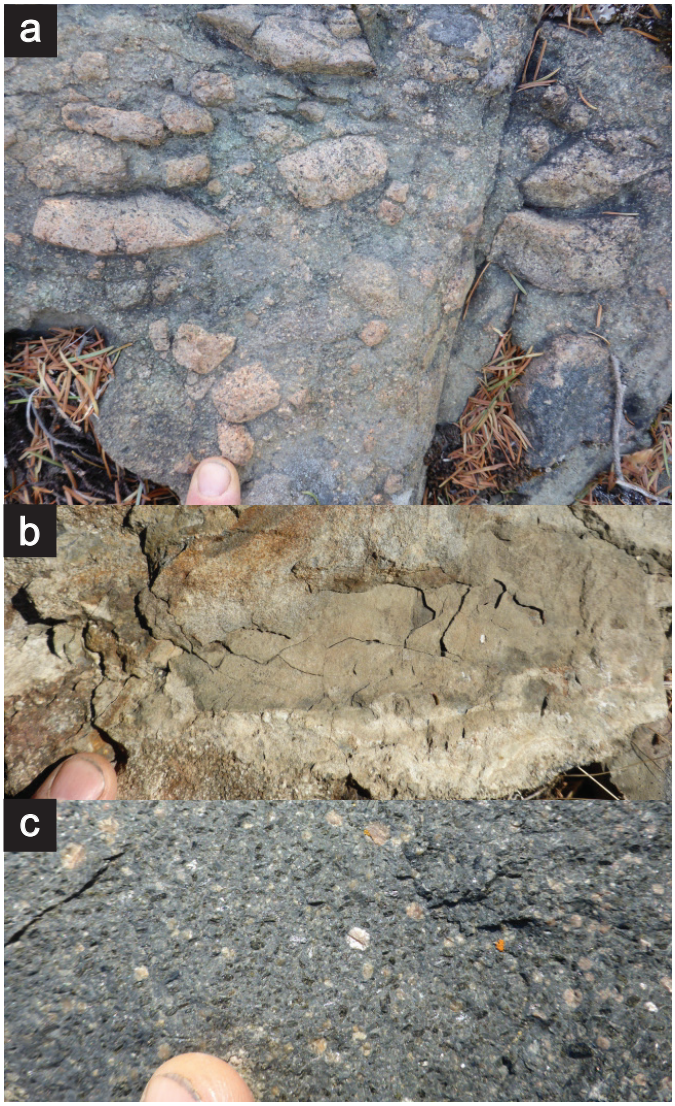

Fig. 7. Three distinctive members of a mappable succession that marks a change in the pyroclastic component of the southern Nicola arc, from hornblende-pyroxene-feldspar-phyric to quartz-apatite-biotite-feldspar-phyric. **a)** Monomictic conglomerate containing round to subangular clasts of orange monzonite. **b)** Light-coloured, calcareous, fine- to coarse-sandstone sampled for MMI17-9-3, surrounds angular, green-brown basalt blocks (limestone bed is mainly below the bottom of the photo). **c)** Basalt with light brown, rounded analcime and black titanaugite phenocrysts in a green-grey matrix.

grain ages ranged from 202.615 ±0.088 to 204.081 ±0.088 Ma (Table 1), and the youngest of these grain ages is herein taken as the time of deposition.

4.3. Upper part of Shrimpton Formation, Highways 97C-5A junction area (MMI18-2-13; Lat. 49.9412°N, Long. -120.5495°E)

Sample MMI18-2-13 was collected from homogeneous ash-tuff bands in well-bedded fossil-bearing calcareous and argillaceous siltstone, interpreted to occupy a position high in the Shrimpton Formation (unit uTrNSHsf, Fig. 3; column III). Tuff-rich outcrop along the westbound Highway 97C roadcut about 4 km east of the junction with Highway 5A (Fig. 2) was exhumed to expose fresh surfaces. From an interval ~25 cm thick we collected ~15 kg of hand-sorted pieces from buff coloured ash-tuff bands up to 8 cm thick (Fig. 8). The tuff bands sampled are interpreted to sit high in the Shrimpton Formation stratigraphy, represent the last gasps of Nicola arc magmatism, subduction cessation, and death of the southern Nicola arc.

The representative population of zircons selected for LA-ICP-MS analysis were clear, high quality, pale pink, squat to slender prisms, only rarely fractured or inclusion-bearing. CL imagery revealed simple internal zoning indicative of magmatic zircon (Friedman et al., 2020; see also examples in Fig. 4). All analyzed grains (n=91) were concordant, within 2-sigma error (Friedman et al., 2020). $^{206}Pb/^{238}U$ dates varied from ca. 215-179 Ma (Fig. 9). Applying a 2-sigma filter resulted in rejection of the five youngest and the two oldest analyses, yielding a weighted mean of $^{206}Pb/^{238}U$ dates at 200.2 ±1.1 Ma. Friedman et al. (2020) argued that minor Pb loss was a likely cause for scatter at the young end of the dataset and grains from the old end of the distribution were likely sourced from slightly older Nicola arc rocks. Thus, the 200.2 Ma age was considered the best age estimate, supported by the tuff age calculator of Isoplot (Ludwig, 2003), which produced an almost identical age: 200.0 +1.2\-1.0 Ma (n=76, 95% level of confidence). Nevertheless, they could not rule out the possibility of a subpopulation of grains centred around 195 Ma.

A selection of the youngest subpopulation grains dated by Friedman et al. (2020) were extracted for CA-TIMS analysis. Grains shown in Table 1 (12-4, 15-2, and 17-5) were 195.8 ±6.4 Ma, 191.7 ±9.4 Ma, and 199.0 ±11.0 Ma, at the low end of the age spectrum used in the weighted average, while grains 4-9 and 18-5 were part of the five rejected young grains falling outside the 2-sigma filter. The new time of deposition from the youngest zircon dated is consistent with the LA-ICP-MS date (200.2 ±1.1 Ma) at the limits of error, but with much improved precision, and an error envelope that is reduced by more than an order of magnitude: 201.304 ±0.086 Ma.

Fig. 8. Light-coloured, feldspar-rich, felsic ash layers within dark brown argillaceous siltstone, sandstone, and rare volcanic pebble conglomerate in the upper part of Shrimpton Formation, record the last pyroclastic eruptions and final gasps of the dying southern Nicola arc. Sample MMI18-2-13 was collected from the outcrop pictured. This sample yielded the youngest age obtained from Nicola Group strata in the study area.

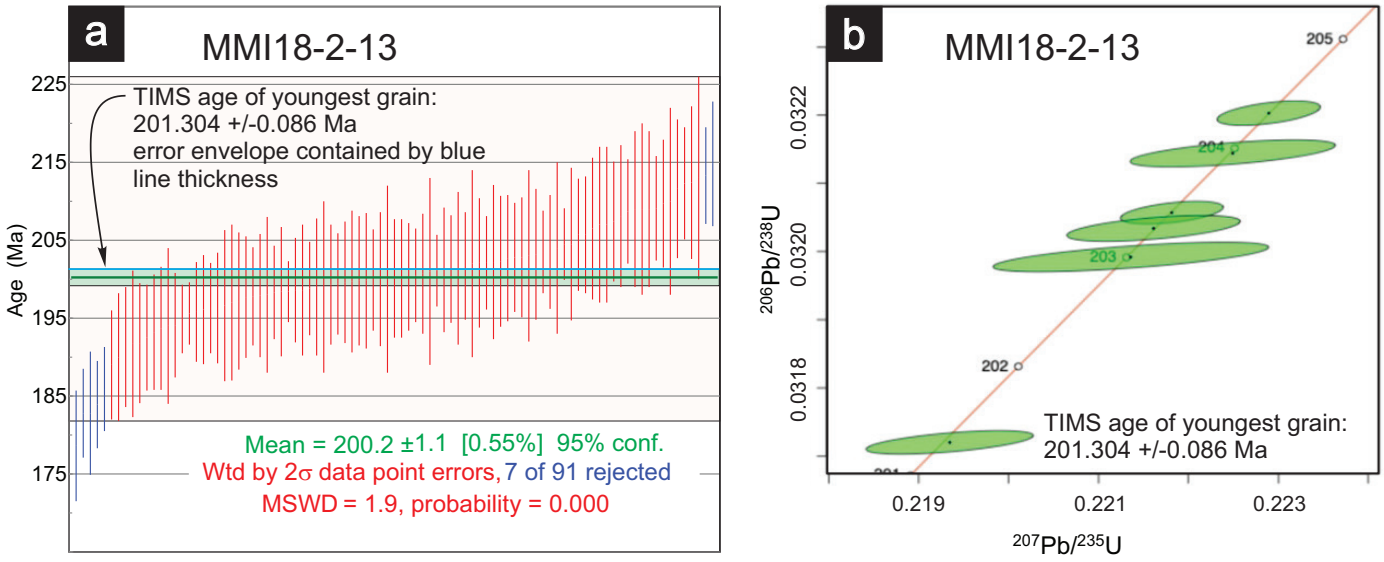

Fig. 9. Comparison of results from **a)** LA-ICP-MS of zircons extracted from sample MMI18-2-13 of a tuff band in the upper part of the Shrimpton Formation and the **b)** CA-TIMS age of the youngest of young representative grains analyzed. In this case, the calculated mean age of all grains ablated (excluding rejects) is the same, at the limit of the reported 2σ error envelope, as the CA-TIMS age (200.2 ±1.1 Ma and 201.304 ±0.086 Ma). Error bounds of this CA-TIMS age overlap those of the age of the Triassic-Jurassic boundary (201.4 ±0.2 Ma; Cohen et al., 2013, rev. 2023).

5. Discussion

In the three cases presented here, high precision TOD determinations are consistent with the MDAs as determined by LA-ICP-MS population mode peaks but provide much greater precision. In all cases the ±2-sigma MDA error envelopes overlap. This provides some confidence in other LA-ICP-MS age determinations based on youngest multigrain age distribution peaks that we have reported for other parts of the Nicola Group stratigraphy (Mihalynuk and Diakow, 2020 and references therein). If the experience with the three TOD ages presented here can be reliably applied to LA-ICP-MS ages of other Nicola arc units, the populations mode is a better representation of the true depositional age than the youngest grain or an average of a small subpopulation of selected young grain ages determined by LA-ICP-MS. Ad hoc methods for selecting youngest grain populations have also been shown to be problematic in other studies where they consistently yield MDAs that are too young (Vermeesch, 2021).

Age constraints from the southern Nicola Group strata suggest that the initiation of Nicola arc was characterized by ca. 13 m.y. of bimodal magmatism (240-227 Ma Missezula Formation; Mihalynuk et al., 2015; Friedman et al., 2020). Widespread, voluminous and rapid outpourings of coarse augite-phyric basalts, a hallmark of the Nicola Group, rapidly inflated the Nicola arc to sea level over 3 m.y. (ca. 227-224 Ma Iron Mountain Formation). This was followed by shallow submarine volcanism with felsic eruptions, this time interbedded with fossiliferous limestone, and locally, reefs (Selish Formation, 224-222 Ma). Coeval with felsic eruptions, granitoid plutons were emplaced, especially near the western magmatic arc axis. Emergence of the Nicola arc was followed by a ca. 15 m.y. period of steady-state volcanism and sedimentation, with deposition of siliciclastic strata that blanketed most of the arc with local coarse hornblende-pyroxene or bladed feldspar-pyroxene volcanic accumulations (Elkhart Formation, 222-207 Ma). This early Nicola arc history reflects our new time of deposition age of 222.036 ±0.086 Ma on the Elkhart Formation suggesting that Elkhart deposition extends to ages approximately 10 m.y. older than previous estimates (Mihalynuk and Diakow, 2020), with the age range of the Selish Formation shrinking accordingly. However, constraints on the minimum age of the Elkhart-Selish contact are still lacking in the eastern part of the study area, so regional diachroneity cannot be ruled out.

Northwest of the study area, early phases of the Guichon batholith were emplaced (217-215 Ma, Whalen et al., 2017) contemporaneously with the Elkhart Formation. Related felsic eruptive centres likely contributed to growth of the arc apron as recorded by the Elkhart Formation and populations of detrital zircons (Mihalynuk and Diakow, 2020 and references within). An abrupt change in pyroclastic mineralogy followed (from pyroxene ±hornblende to the addition of biotite-apatite-quartz), and this petrographic change marks the base of the succeeding Shrimpton Formation (207-201 Ma).

Our preferred interpretation of the Shrimpton-Elkhart formations contact is as a diachronous surface, likely deposited during deformation of the Nicola arc. It is marked by a period of exhumation of foliated gabbroic infrastructure of the Nicola arc. Clasts derived from the deformed gabbros were incorporated into the upper Elkhart Formation conglomerate. Locally the entire Elkhart sedimentary apron was removed, and Shrimpton Formation was deposited directly on Iron Mountain Formation. Details of this deformation event are not easily resolved, in part because only the uppermost crustal section

did not develop tectonic fabrics and any fabrics that may have developed are overprinted by a subsequent deformation. However, this deformation may mark a diachronous transition to Shrimpton Formation deposition (ca. 209-207 Ma; following youngest cooling age on Elkhart volcanic strata, ca. 210 Ma in Mihalynuk et al., 2025). Elkhart strata containing foliated gabbroic boulders have not yet been precisely dated, but if this early deformation/exhumation timing is correct, it is coeval with the transition from unmineralized to mineralized porphyry copper-molybdenum-bearing phases of the calc-alkalic Guichon batholith (ca. 208.5 Ma; Ash et al., 2007; D'Angelo et al., 2017; Whalen et al., 2017).

The Shrimpton Formation (<207-201.304 ±0.086 Ma) is coeval with alkalic-style copper-silver-gold porphyry mineralization of the Copper Mountain suite (ca. 206-201 Ma; Logan et al., 2007; Mihalynuk et al., 2010; Logan and Mihalynuk, 2014) located to the east of the axis of calc-alkalic magmatism. A belt of small dioritic intrusions distributed longitudinally along the axis of the study area have been correlated with the Copper Mountain suite (Preto, 1972, 1979; Mihalynuk and Diakow, 2020), and mineralized portions of the suite contain conspicuous concentrations of apatite, biotite and magnetite similar to Shrimpton Formation pyroclastic rocks. For example, magnetite-apatite dikes are associated with the main porphyry mineralizing event displayed in the open pit at the Afton deposit, and magnetite-biotite-K-feldspar alteration is ubiquitous at Copper Mountain and Afton (Logan and Mihalynuk, 2014). Monzonite and diorite are important syn-mineralization host rocks at both deposits with parallels in the porphyritic monzonitic conglomerates and alkaline analcime basalt flows, both diagnostic units of the Shrimpton Formation succession. Evaluating petrogenetic associations between late Elkhart-Shrimpton volcanism and whatever arc event(s) was/were responsible for the formation of copper porphyry mineralization is beyond the scope of this report. However, Logan and Mihalynuk (2014) hypothesized that generation of hydrated, copper-rich magmas was a consequence of collision of an extinct Permian-Middle Triassic Kutcho-Sitlika-Wineglass arc (Schiarizza, 2013) that was lodged in the plate (cf. Logan and Mihalynuk, 2014) subducting beneath the Nicola arc in the Late Norian to Early Rhaetian (see also Mihalynuk and Diakow, 2020).

Even though uplift, deep arc erosion, and local preservation of pre-Shrimpton deformational fabrics point to regional deformation ca. 209-207 Ma, most evidence of contractional deformation in the study area is younger. The best examples of thrust and fold belt deformation involve Shrimpton Formation. Thus, the age of this deformation is bracketed between 201 and 193 Ma by the time of deposition of the upper part of the Shrimpton Formation (201.304 ±0.086 Ma) and the ca. 193 Ma Pennask batholith, which cuts the folds and thrust faults (Mihalynuk et al., 2016).

The question of whether Nicola Group magmatism extends into the Jurassic remains unresolved. Friedman et al. (2020) claimed that it did, based on their LA-ICP-MS zircon age determination of 200.2 ±1.1 Ma from tuff bands in Shrimpton Formation, as compared to the IUGS timescale calibration for the Triassic-Jurassic boundary at 201.3 ±0.2 Ma (Cohen et al., 2013, rev. 2019). However, our new TOD for the same tuff layers point to an age of 201.304 ±0.084 Ma which is on the old side of the Cohen et al. (2013, rev. 2019) boundary. However, our new TOD is on the young side of the most recently revised Triassic-Jurassic boundary at 201.4 ±0.2 Ma (moved 0.1 m.y. older in Cohen et al., 2013, rev. 2023). At the combined limits of error (201.39 vs. 201.2 Ma), the upper Shrimpton Formation tuff bands sampled could be Rhaetian (latest Triassic). However, as mentioned by Friedman et al. (2020), an Early Jurassic age would support persistent failed attempts to extract conodont elements (jaw parts of eel-like cordates of the class Conodonta, that disappeared at the end of the Triassic; Sweet and Donoghue, 2001) from samples collected from biogenic limestone beds within the upper Shrimpton Formation.

6. Summary

We show that the population mode of LA-ICP-MS detrital zircon age spectra yield statistical ages consistent with the time of deposition as determined by high precision CA-TIMS on the youngest igneous grains in three Nicola arc samples. The time of deposition for key stratigraphic intervals of the Nicola Group bracket the time when most of the porphyry copper mineralization in the southern Nicola arc formed. This mineralizing epoch follows the main arc constructional phase (227-222 Ma) through its emergence above sea level (222-210 Ma). In the western Nicola arc, this emergence is now dated between 224 Ma and the new time of deposition age of 222.036 ±0.086 Ma. Ages of regional porphyry copper mineralization (209-204 Ma) in the southern Nicola arc overlap a major change in phenocryst assemblage, from pyroxene to biotite and apatite, presumably related to increased hydration of copper-laden magmas (ca. 207-203 Ma). At the same time, outpourings of alkalic, analcime basalt flows suggest that a deep, primitive source region was tapped (new TOD is 202.615 ±0.088 Ma). Sparse tuff layers high in the Shrimpton stratigraphy record the last gasps of Nicola arc magmatism (new TOD is 201.304 ±0.084 Ma), immediately before the terminal Triassic (ca. 201 Ma; Cohen et al., 2013, rev. 2023).

Acknowledgments

Larry Diakow (British Columbia Geological Survey, retired) was instrumental in delivering the Southern Nicola Arc Project (2013-2020). James Logan (British Columbia Geological Survey, retired) was a key proponent during launch of the project and in establishing geological and metallogenetic relationships in the southern half of the study area (2012-2014). Yao Cui contributed to field studies and sample collection (2017-2018). Martha Henderson, Johannes Jakob, Theron Findley, and Gerri McEwan ably contributed to mapping and field support. We thank Jeffrey Chiarenzelli (St. Lawrence University) and Luke Ootes (British Columbia Geological Survey) for reviews that improved this contribution.

References cited

Archibald, D.A., Glover, J.K., Price, R.A., Farrar, E., and Carmichael, D.M., 1983. Geochronology and tectonic implications of magmatism and metamorphism, southern Kootenay arc and neighbouring regions, southeastern British Columbia, Part 1: Jurassic to mid-Cretaceous. Canadian Journal of Earth Sciences, 20, 1891-1913.

Ash, C.H., Reynolds, P.H., Creaser, R.A., and Mihalynuk, M.G., 2007. $^{40}Ar/^{39}Ar$ and Re-O isotopic ages for hydrothermal alteration and related mineralization at the Highland Valley Cu-Mo deposit (NTS 092I), southwestern British Columbia. In: Geological Fieldwork 2006, British Columbia Ministry of Energy, Mines and Petroleum Resources, British Columbia Geological Survey Paper 2007-1, pp. 19-24.

Barr, D.A., Fox, P.E., Northcote, K.E., and Preto, V.A., 1976. The Alkaline Suite Porphyry Deposits-A Summary. In: Porphyry Deposits of the Canadian Cordillera. Sutherland Brown, A., (Ed.), Canadian Institute of Mining and Metallurgy, Special Volume 15, pp. 359-367.

Black, L.P., Kamo, S.L., Allen, C.M., Davis, D.W., Aleinikoff, J.N., Valley, J.W., Mundil, R., Campbell, I.H., Korsch, R.J, Williams, I.S., and Foudoulis, C., 2004. Improved $^{206}Pb/^{238}U$ microprobe geochronology by the monitoring of a trace-element-related matrix effect; SHRIMP, ID-TIMS, ELA-ICP-MS and oxygen isotope documentation for a series of zircon standards. Chemical Geology, 205, 115-140.

Cohen, K.M., Finney, S.C., Gibbard, P.L., and Fan, J.-X., 2013; revs. 2019, 2023. The ICS International Chronostratigraphic Chart. Episodes 36, 199-204. <https://stratigraphy.org/ICSchart/ChronostratChart2023-04.pdf>

Colpron, M., 2020. Yukon terranes-A digital atlas of terranes for the northern Cordillera. Yukon Geological Survey. <https://data.geology.gov.yk.ca/Compilation/2#InfoTab>

Colpron, M., and Nelson, J.L., 2011. A digital atlas of terranes for the northern Cordillera. British Columbia Ministry of Energy and Mines, British Columbia Geological Survey GeoFile 2011-11.

Colpron, M., Warren, M.J., and Price, R.A., 1998. Selkirk fan structure, southeastern Canadian Cordillera: Tectonic wedging against an inherited basement ramp. Geological Society of America Bulletin, 110, 1060-1074.

Coney, P.J., Jones, D.L., and Monger, J.W., 1980. Cordilleran suspect terranes. Nature, 288, 329-333.

Condon, D.J., Schoene, B., McLean, N.M., Bowring, S.A., and Parrish, R.R., 2015. Metrology and traceability of U-Pb isotope dilution geochronology (EARTHTIME Tracer Calibration Part I). Geochimica et Cosmochimica Acta, 164, 464-480.

Crowley, J.L., Schoene, B., and Bowring, S.A. 2007. U-Pb dating of zircon in the Bishop Tuff at the millennial scale. Geology, 35, 1123-1126.

D'Angelo, M., Miguel, A., Hollings, P., Byrne, K., Piercey, S., and Creaser, R.A., 2017. Petrogenesis and magmatic evolution of the Guichon Creek batholith: Highland Valley porphyry Cu ±(Mo) district, south-central British Columbia. Economic Geology, 112, 1857-1888. <https://doi.org/10.5382/econgeo.2017.4532>

Eggins S.M., Kinsley L., and Shelley J., 1998. Deposition and element fractionation processes during atmospheric pressure laser sampling for analysis by ICP-MS. Applied Surface Science, 127, 278-286.

Friedman, R.M., Mihalynuk, M.G., Diakow, L.J., and Gabites, J.E., 2016. Southern Nicola Arc Project 2015: Geochronologic data constraining Nicola Arc history along a transect near 50°N. British Columbia Ministry of Energy and Mines, British Columbia Geological Survey GeoFile 2016-03, 19 p.

Friedman, R.M., Mihalynuk, M.G., and Diakow, L.J., 2020. Geochronologic data from samples collected near Pothole Lake and Pennask Mountain (NTS 92H/15, 16) as part of the Southern Nicola Arc Project. British Columbia Ministry of Energy, Mines and Low Carbon Innovation, British Columbia Geological Survey GeoFile 2020-12, 6 p.

Gabites, J., and Mihalynuk, M.G., 2025. $^{40}Ar/^{39}Ar$ geochronologic data from samples collected as part of the Southern Nicola Arc Project. British Columbia Ministry of Mining and Critical Minerals, British Columbia Geological Survey GeoFile, in press.

Gehrels, G., 2014. Detrital zircon U-Pb geochronology applied to tectonics. Annual Review of Earth and Planetary Sciences, 42, 127-149.

Gerstenberger, H., and Haase, G., 1997. A highly effective emitter substance for mass spectrometric Pb isotopic ratio determinations. Chemical Geology, 136, 309-312.

Herriott, T.M., Crowley, J.L., Schmitz, M.D., Wartes, M.A., Gillis, R.J., 2019. Exploring the law of detrital zircon: LA-ICP-MS and CA-TIMS geochronology of Jurassic forearc strata, Cook Inlet, Alaska, USA. Geology, 47, 1044-1048. <https://doi.org/10.1130/G46312.1>

Hiess, J., Condon, D.J., McLean, N., and Noble, S.R., 2012. $^{238}U/^{235}U$ systematics in terrestrial uranium-bearing minerals. Science, 335, 1610-1614.

Jaffey, A.H., Flynn, K.F., Glendenin, L.E., Bentley, W.C., and Essling, A.M., 1971. Precision measurement of half-lives and specific activities of ^{235}U and ^{238}U. Physics Review, C4, 1889-1906.

Krogh, T.E., 1973. A low-contamination method for hydrothermal decomposition of zircon and extraction of U and Pb for isotopic age determinations, Geochimica et Cosmochimica Acta, 37, 485-494. <https://doi.org/10.1016/0016-7037(73)90213-5>

Logan, J.M., and Mihalynuk, M.G., 2014. Tectonic controls on early Mesozoic paired alkaline porphyry deposit belts (Cu-Au ±Ag-Pt-Pd-Mo) within the Canadian Cordillera. Economic Geology, 109, 827-858.

Logan, J.M., Mihalynuk, M.G., Ullrich, T., and Friedman, R.M., 2007. U-Pb ages of intrusive rocks and $^{40}Ar/^{39}Ar$ plateau ages of copper-gold-silver mineralization associated with alkaline intrusive centres at Mount Polley and the Iron Mask batholith, southern and central British Columbia. In: Geological Fieldwork 2006, British Columbia Ministry of Energy, Mines and Petroleum Resources, British Columbia Geological Survey Paper 2007-1, pp. 93-116.

Lowell, J.D., and Guilbert, J.M., 1970. Lateral and vertical alteration-mineralization zoning in porphyry ore deposits. Economic Geology, 65, 373-408.

Ludwig, K.R., 2003. Isoplot 3.09: A geochronological toolkit for Microsoft Excel. Berkeley Geochronology Center, Special Publication 4, Berkeley.

Mattinson, J.M., 2005. Zircon U-Pb chemical abrasion (CA-TIMS) method: Combined annealing and multi-step partial dissolution analysis for improved precision and accuracy of zircon ages. Chemical Geology, 220, 47-66.

McMillan, W.J., 1981. Nicola Project-Merritt Area. British Columbia Department of Mines, Preliminary Map 47, 1:25,000 scale, 2 sheets.

McMillan, W.J., and Panteleyev, A., 1980. Ore deposit models-1. Porphyry copper deposits. Geoscience Canada, 7, 52-63.

Mihalynuk, M.G., and Diakow, L.J., 2020. Southern Nicola arc geology (NTS 92H/7NE, 8NW, 9W, 10E, 15E, 16W, 92I/1SW, 2SE). British Columbia Ministry of Energy, Mines and Low Carbon Innovation, British Columbia Geological Survey Geoscience Map 2020-01, 1:50,000 scale, 2 sheets.

Mihalynuk, M.G., Nelson, J., and Diakow, L.J., 1994. Cache Creek Terrane entrapment: oroclinal paradox within the Canadian Cordillera. Tectonics, 13, 575-595.

Mihalynuk, M.G., Erdmer, P., Ghent, E.D., Cordey, F., Archibald, D.A., Friedman, R.M., and Johannson, G.G., 2004. Coherent French Range blueschist: Subduction to exhumation in <2.5 m.y.? Geological Society of America Bulletin, 116, 910-922. <https://doi.org/10.1130/B25393.1>

Mihalynuk, M.G., Logan, J.M., Friedman, R.M., and Preto, V.A., 2010. Age of mineralization and "Mine Dykes" at Copper Mountain alkaline copper-gold-silver porphyry deposit (NTS 092H/07), south-central British Columbia. In: Geological Fieldwork 2009, British Columbia Ministry of Energy and Mines, British Columbia Geological Survey Paper 2010-1, pp. 163-171.

Mihalynuk, M.G., Logan, J.M., Diakow, L.J., Henderson, M.A., Jacob, J., and Watson, A.K.G., 2014a. Summers Creek area preliminary geology (NTS 092H/9W & 10E). British Columbia Ministry of Energy and Mines, British Columbia Geological Survey Open File 2014-05.

Mihalynuk, M.G., Logan, J.M., Diakow, L.J., Friedman, R.M., and Gabities, J., 2014b. Southern Nicola Arc Project (SNAP): Preliminary results. In: Geological Fieldwork 2013, British Columbia Ministry of Energy and Mines, British Columbia Geological Survey Paper 2014-1, pp. 29-57.

Mihalynuk, M.G., Friedman, R.M., Gabites, J.E., and Logan, J.M., 2014c. Southern Nicola Arc Project 2013: Geochronological data. British Columbia Ministry of Energy and Mines, British Columbia Geological Survey, GeoFile 2014-3, 7 p.

Mihalynuk, M.G., Diakow, L.J., Logan, J.M., and Friedman, R.M., 2015a. Preliminary geology of the Shrimpton Creek area (NTS 092H/15E, 16W) Southern Nicola Arc Project. In: Geological Fieldwork 2014, British Columbia Ministry of Energy and Mines, British Columbia Geological Survey Paper 2015-1, pp. 129-163.

Mihalynuk, M.G., Friedman, R.M., and Logan, J.M., 2015b. Southern Nicola Arc Project 2014: Geochronological data. British Columbia Ministry of Energy and Mines, British Columbia Geological Survey, GeoFile 2015-02, 7 p.

Mihalynuk, M.G., Diakow, L.J., Friedman, R.M., and Logan, J.M., 2016. Chronology of southern Nicola arc stratigraphy and deformation. In: Geological Fieldwork 2015, British Columbia Ministry of Energy and Mines, British Columbia Geological Survey Paper 2016-1, pp. 31-63.

Mihalynuk, M.G., Friedman, R.M., and Wall, C., 2025. U-Pb Geochronologic data from samples collected as part of the Southern Nicola Arc Project. British Columbia Ministry of Mining and Critical Minerals, British Columbia Geological Survey, GeoFile 2025, in press.

Monger, J.W.H., Price, R.A., and Tempelman-Kluit, D.J., 1982. Tectonic accretion and the origin of the two major metamorphic and plutonic welts in the Canadian Cordillera. Geology, 10, 70-75.

Monger, J.W.H., 1989. Geology, Hope, British Columbia. Geological Survey of Canada, Map 41-1989, 1:250,000 scale.

Monger, J.W.H., and McMillan, W.J., 1989. Geology, Ashcroft, British Columbia. Geological Survey of Canada, Map 42-1989, 1:250,000 scale.

Nixon, G., Scheel, E.J., Scoates, J., Friedman, R.M., Wall, C.J., Gabites, J., and Jackson-Brown, S., 2020. Syn-accretionary multi-stage assembly of an Early Jurassic Alaskan-type intrusion in the Canadian Cordillera: U-Pb and $^{40}Ar/^{39}Ar$ geochronology of the Turnagain ultramafic-mafic intrusive complex, Yukon-Tanana terrane. Canadian Journal of Earth Sciences, 57, 575-600.

Orchard, M.J., 1990. Report on conodonts and other microfossils, Hope (92H), 34 collections made by G.E. Ray, British Columbia Geological Survey, 1981, 1985-1987. Unpublished.

Patton, C., Hellstrom, J., Paul, B., Woodhead, J., and Hergt, J., 2011. Iolite: Freeware for the visualization and processing of mass spectrometry data. Journal of Analytical Atomic Spectroscopy, 26, 2508-2518.

Preto, V.A., 1972. Geology of Copper Mountain. British Columbia Department of Mines and Petroleum Resources, Geological Division Bulletin 59, 95 p.

Preto, V.A., 1979. Geology of the Nicola Group between Merritt and Princeton: British Columbia Ministry of Energy, Mines and Petroleum Resources, Geological Division Bulletin 69, 90 p.

Schau, M.P., 1968. Geology of the Upper Triassic Nicola Group in south central British Columbia. Unpublished Ph.D. Thesis, The University of British Columbia, Vancouver, Canada, 211 p.

Schiarizza, P., 2013. The Wineglass assemblage, lower Chilcotin River, south-central British Columbia: Late Permian volcanic and plutonic rocks that correlate with the Kutcho assemblage of northern British Columbia. In: Geological Fieldwork 2012, British Columbia Ministry of Energy, Mines and Natural Gas, British Columbia Geological Survey Paper 2013-1, pp. 53-70.

Schiarizza, P., 2019. Geology of the Nicola Group in the Bridge Lake-Quesnel River area, south-central British Columbia. In: Geological Fieldwork 2018, British Columbia Ministry of Energy, Mines and Petroleum Resources, British Columbia Geological Survey Paper 2019-01, pp. 15-30.

Schmitz, M.D., and Schoene, B., 2007. Derivation of isotope ratios, errors, and error correlations for U-Pb geochronology using ^{205}Pb-^{235}U(^{233}U)-spiked isotope dilution thermal ionization mass spectrometric data. Geochemistry, Geophysics, Geosystems, 8. <https://agupubs.onlinelibrary.wiley.com/doi/pdf/10.1029/2006GC001492>

Sláma, J., Kosler, J., Condon, D.J., Crowlley, J.L., Gerdes, A., Hanchar, J.M., Horstwood, M.S.A., Morris, G.A., Nasdala, L., Norberg, N., Schaltegger, U., Xchoene, B., Tubrett, M.N., and Whitehouse, M.J., 2008. Plesovice zircon-A new natural reference material for U-Pb and Hf isotopic microanalysis. Chemical Geology, 249, 1-35.

Sweet, W.C., and Donoghue, P.C., 2001. Conodonts: past, present, future. Journal of Paleontology, 75, 1174-1184.

Vermeesch, P., 2018, IsoplotR: A free and open toolbox for geochronology. Geoscience Frontiers, 9, 1479-1493. <https://doi.org/10.1016/j.gsf.2018.04.001>

Vermeesch, P., 2021. Maximum depositional age estimation revisited. Geoscience Frontiers, 12, 843-850. <https://doi.org/10.1016/j.gsf.2020.08.008>

Wiedenbeck, M., Alle, P., Corfu, F., Griffin, W.L., Meier, M., Oberli, F., Quadt, A.V., Roddick, J.C., and Spiegel, W., 1995. Three natural zircon standards for U-Th-Pb, Lu-Hf, trace element and REE analyses. Geostandards Newsletter, 19, 1-23.

Whalen, J.B., Davis, W.J., and Anderson, R.G., 2017. Temporal and geochemical evolution of the Guichon Creek Batholith and Highland Valley porphyry copper district, British Columbia: Implications for generation and tectonic setting of porphyry systems. Geological Survey of Canada, Open File, 8334, 49 p.

Wheeler, J.O., and McFeely, P., 1987. Tectonic assemblage map of the Canadian Cordillera and adjacent parts of the United States of America. Geological Survey of Canada. Geological Survey of Canada, Open File 1565, 1:2,000,000 scale.

Wheeler, J.O., Brookfield, A.J., Gabrielse, H., Monger, J.W.H., Tipper, H.W., and Woodsworth, G.J., 1991. Terrane map of the Canadian Cordillera, Geological Survey of Canada, "A" Series Map 1713A, 1:2,000,000 scale, 2sheets. <https://doi.org/10.4095/133550>

Zagorevski, A., van Staal, C.R., Bédard, J.H., Bogatu, A., Canil, D., Coleman, M., Golding, M., Joyce, N.L., Lawley, C., McGoldrick, S., Mihalynuk, M.G., Milidragovic, D., Parsons, A., and Schiarizza, P., 2021. Overview of Cordilleran oceanic terranes and their significance for the tectonic evolution of the northern Cordillera. In: Ryan, J.J., and Zagorevski, A., (Eds.), Northern Cordillera geology: a synthesis of research from the Geo-mapping for Energy and Minerals program, British Columbia and Yukon. Geological Survey of Canada, Bulletin 610, pp. 21-65.